UCSF
UC San Francisco Previously Published Works

Title
Comparison of quantitative susceptibility mapping methods on evaluating radiation-induced cerebral microbleeds and basal ganglia at 3T and 7T.

Permalink
https://escholarship.org/uc/item/07w4x2qn

Journal
NMR in Biomedicine, 35(5)

Authors
Chen, Yicheng
Genc, Ozan
Poynton, Clare
et al.

Publication Date
2022-05-01

DOI
10.1002/nbm.4666

Peer reviewed

eScholarship.org Powered by the California Digital Library
University of California

Author Manuscript

Author Manuscript

Author Manuscript

Author Manuscript

HHS Public Access

Author manuscript

NMR Biomed. Author manuscript; available in PMC 2023 August 22.

Published in final edited form as:

NMR Biomed. 2022 May ; 35(5): e4666. doi:10.1002/nbm.4666.

Comparison of Quantitative Susceptibility Mapping Methods on Evaluating Radiation Induced Cerebral Microbleeds and Basal Ganglia at 3T and 7T

Yicheng Chen[1,2], **Ozan Genc**[2,3], **Clare B. Poynton**[2], **Suchandrima Banerjee**[4], **Christopher P. Hess**[2,5], **Janine M. Lupo**[1,2]

[1]UC Berkeley-UCSF Graduate Program in Bioengineering, University of California, Berkeley and San Francisco, CA

[2]Department of Radiology and Biomedical Imaging, University of California, San Francisco, CA

[3]Institute of Biomedical Engineering, Boğaziçi University, Istanbul, Turkey

[4]GE Healthcare, Menlo Park, CA

[5]Department of Neurology, University of California, San Francisco, CA

Abstract

Quantitative susceptibility mapping (QSM) has the potential of being a biomarker for various diseases because of its ability to measure tissue susceptibility related to iron deposition, myelin, and hemorrhage from the phase signal of a T2*-weighted MRI. Despite its promise as a quantitative marker, QSM is faced with many challenges, including its dependence on preprocessing of the raw phase data, the relatively weak tissue signal, and the inherently ill-posed relationship between the magnetic dipole and measured phase. The goal of this study was to evaluate the effects of background field removal and dipole inversion algorithms on noise characteristics, image uniformity, and structural contrast for CMB quantification at both 3T and 7T. We selected four widely used background phase removal and five dipole field inversion algorithms for QSM and applied them to patients with cerebral microbleeds (CMB) who were scanned at two different field strengths and volunteers with ground truth QSM reference calculated using multiple orientation scans. 7T MRI provided QSM images with lower noise than 3T MRI. QSIP and VSHARP + iLSQR achieved the highest white matter homogeneity and vein contrast, with QSIP also providing the highest CMB contrast. Compared to ground truth COSMOS QSM images, overall good correlations between susceptibility values of dipole inversion algorithms and the COSMOS reference were observed in basal ganglia regions, with VSHARP + iLSQR achieving the most similar susceptibility values to COSMOS across all regions. This study can provide guidance for selecting the most appropriate QSM processing pipeline based on the application of interest and scanner field strength.

Corresponding author: Janine M. Lupo, Address: Byers Hall UCSF, Box 2532, 1700 4th Street, Suite 303D, San Francisco, CA 94158-2330, USA, Janine.Lupo@ucsf.edu, Tel: +1 (415) 502-0646, Fax: +1 (415) 514-1028.

Author Manuscript Author Manuscript Author Manuscript Author Manuscript

Keywords

Magnetic resonance imaging (MRI); Quantitative susceptibility mapping (QSM); Background phase removal; Dipole field inversion; cerebral microbleeds (CMBs); Basal ganglia

Introduction

Quantitative susceptibility mapping (QSM) has shown great promise in quantifying tissue susceptibility, a physical property in vivo that is related to tissue molecular composition, using image phase signal from gradient echo MRI[1,2]. Due to its quantitative nature, QSM has been adopted to investigate many neurodegenerative and vascular diseases, including hemorrhage[3], ischemic stroke[4], Multiple Sclerosis (MS)[5], Parkinson's disease (PD)[6], Alzheimer's disease (AD)[7], Huntington's disease (HD)[8], and amyotrophic lateral sclerosis (ALS)[9]. Although MR susceptibility-weighted imaging (SWI) has been readily adopted to investigate the formation of hemosiderin-containing cerebral microbleeds (CMBs) that are present in many vascular disorders[10–12], the qualitative nature of the SWI processing along with the blooming artifact that results from T2* dephasing of the underlying magnitude image[13] makes QSM an attractive alternative for accurate quantification of CMB volume[14] and delineation of vascular structures. Due to its high sensitivity and quantitative ability to measure susceptibility sources such as iron in the brain, QSM has also become an effective *in vivo* approach for quantifying the spatial distribution of iron, especially in deep brain nuclei or basal ganglia. The progressive accumulation of iron in these regions is evident in normal aging[15] and has been shown to be accelerated in multiple neurodegenerative disorders. As examples, He et al. found increased susceptibility within substantia nigra and red nucleus contralateral to the most affected limb in the early PD patients compared to healthy controls[6]; Acosta-Cabronero et al. reported susceptibility differences within the putamen and posterior temporo-parietal white matter of AD patients[7]; and Van Bergen et al. demonstrated significantly elevated susceptibility in the caudate nucleus, putamen, globus pallidus, and substantia nigra between subjects with premanifest HD compared to age-matched controls that correlated with genetic burden score[8]. These studies and others support the role of susceptibility as a biomarker for early diagnosis of disease onset and monitoring of disease progression[16].

Despite the encouraging results obtained using QSM, the methodology itself suffers from several limitations that limit its widespread clinical adoption. These remain the topic of ongoing investigation. Most pipelines for generating QSM images are comprised of 2 main processes: background field removal and dipole inversion. The first step in generating a uniform QSM image of brain tissue involves the accurate removal of background phase, which is derived from susceptibility sources external to the brain, such as the environment and air-tissue interfaces[17]. Since in most cases the background phase is 1 to 2 orders of magnitude stronger than the tissue phase, a robust background removal algorithm is required to extract tissue phase from the total phase signal[18–21]. The second step typically involves employing a method to efficiently perform dipole inversion, whereby the net magnetic field perturbation within any given voxel is represented by the superposition of all dipole fields generated by all voxels. This step is the most computationally intensive because it is

Author Manuscript Author Manuscript Author Manuscript Author Manuscript

calculated by a point-wise multiplication in frequency space followed by solving the inverse problem ($\Delta B_z(\boldsymbol{k}) = B_0\left(\frac{1}{3} - \frac{k_z^2}{|\boldsymbol{k}|^2}\right)\chi\left(\boldsymbol{k}\right)$) to estimate the susceptibility field, where ΔB_z is the local field perturbation, B_0 is the main magnetic field, χ represents the tissue susceptibility, $\boldsymbol{k}$ is the frequency space vector and k_z is the z-component. When $k_z^2/|\boldsymbol{k}|^2 \approx 1/3$, which is commonly referred as the "zero-cone region", the bracket term on the right-hand side becomes close to zero, causing either missing measurements or noise amplification when solving the inverse problem. One approach to avoid this inherently ill-posed problem is to acquire phase data with 3 or more different B_z directions and fill in the missing data near the zero-cone[22]. Although this method, known as COSMOS, is considered the gold-standard for producing highly accurate artifact-free results, it is clinically impractical because of the prolonged scan times, uncomfortable head positioning, and computational requirements. As a result, modern QSM methods typically rely on either: 1) dipole inversion algorithms to solve the ill-posed inversion problem after background field removal[21,23–26], or 2) algorithms that integrate the two steps to reduce the error propagation between consecutive processing steps[27,28].

Despite its promise as quantitative biomarker in the diagnosis and monitoring numerous pathologies, QSM has not yet achieved routine clinical application because of the above technical challenges, lengthy computation times, lack of widespread algorithm availability, and need for fine-tuning of parameters for a given acquisition and set up. Although a variety of algorithms and approaches have been proposed to tackle these challenges, the accuracy of these methods and the resulting quality of QSM images have not been quantitatively assessed in a clinical setting. The goal of this study was to evaluate the effects of applying different background field removal and dipole inversion algorithms on noise characteristics, image uniformity, and structural contrast for CMB quantification of QSM images acquired at 3T and 7T field strengths. To accomplish this, we selected four widely-used background phase removal and five diverse types of dipole field inversion algorithms for QSM and applied them to 11 patients with CMBs and 8 volunteers with ground truth QSM reference calculated using multiple-orientation scans.

Materials and Methods

Subjects and Image Acquisition

Two groups of subjects were recruited for this study. The first consisted of 11 patients (mean age = 35.4 years) with high grade gliomas who received radiation therapy between 2 and 15 years before imaging and developed cerebral microbleeds as a result of their treatment. This group of patients were scanned on both 3T and 7T MRI scanners (GE Healthcare Technologies, Milwaukee, WI, USA) on the same day less than 30 minutes apart. The second group consisted of 8 healthy volunteers (mean age=28 years) scanned only on a 7T MRI scanner. This study was approved by our Committee of Human Research, and written informed consent was obtained from all subjects. The image acquisition parameters for the two groups were as follows:

Author Manuscript Author Manuscript Author Manuscript Author Manuscript

1. Group 1: High resolution T2*-weighted spoiled gradient (SPGR) echo sequence with 3D flow-compensation was performed using whole-body 3T and 7T MRI scanners with 8-channel phased array coils. TE/TR was 28/46ms at 3T and 16/50ms at 7T. A two-fold(3T)/three-fold(7T) generalized auto-calibrating partial parallel acquisition (GRAPPA) with 16 auto-calibrating lines was implemented to keep the total acquisition within 7min[29]. A 24cm FOV, 0.5×0.5×2mm resolution and flip angle of 20°were used at both field strengths. This protocol had been empirically determined previously to result in superior detection of CMBs.

2. Group 2: 3D multi-echo gradient-recalled sequence (4 echoes, TE= 6/9.5/13/16.5ms, TR=50ms, FA=20°, bandwidth=50kHz, 0.8mm isotropic resolution, FOV=24×24×15cm) was performed using a 32-channel phase-array coil on the 7T MRI scanner. The sequence was repeated three times on each volunteer with different head orientations (normal position, head tilted forward and tilted left) to acquire data for COSMOS reconstruction. Autocalibrated Reconstruction[30], a self-calibrated data-driven parallel imaging with an acceleration factor of 3 and 16 auto-calibration lines were also adopted to reduce the scan time of each orientation to about 17 minutes.

Image Reconstruction and Preprocessing

The raw complex k-space data were transferred from the scanner to a Linux workstation, where image reconstruction was performed off-line using an in-house program based on MATLAB 2015b (MathWorks, Natick, MA). The reconstruction pipeline for the single-echo SPGR and multi-echo sequences is demonstrated in Figure 1. Missing phase-encoding lines were filled in using the auto-calibrating reconstruction for Cartesian sampling (ARC) method for each individual coil[30] and then a channel-wise inverse Fourier transform was applied to obtain the coil magnitude and phase images. Coil images were combined using the Multi-Channel-Phase-Combination-3D-Simplified (MCPC-3D-S) method[31] to obtain robust magnitude and raw phase images for each echo. For the multi-echo sequence used for group 2, this process was performed individually on each echo and repeated orientation scan. Skull stripping and brain mask extraction were applied to the magnitude image using FMRIB Software Library (FSL) Brain Extraction Tool (BET)[32]. For the multi-echo sequence, BET was applied to magnitude images generated separately from each of four echoes and the final brain mask was generated by calculating the intersection of all the masks. Since the raw phases acquired from k-space data is constrained to $-\pi$-$+\pi$ range, a 3D Laplacian phase unwrapping method[2] was applied on the phase image and both the unwrapped phase image and Laplacian image were saved for subsequent QSM processing.

QSM Processing

Background Field Removal Algorithms—The background removal and dipole inversion algorithms selected for comparison in this study are summarized in Table 1. From the variety of background phase removal algorithms, we selected the following four commonly used and readily available methods for evaluation and comparison:

Author Manuscript Author Manuscript Author Manuscript Author Manuscript

1. **PDF**: Projection onto Dipole Fields[19], included in MEDI toolbox provided by Cornell MRI Research Lab (http://pre.weill.cornell.edu/mri/pages/qsm.html) and applied on unwrapped phase images.

2. **RESHARP**: Regularization-Enabled Sophisticated Harmonic Artifact Reduction for Phase data[20], implemented in Matlab 2015b according to the published paper and applied on unwrapped phase images. We chose the radius of the spherical convolution kernel as 6 voxels.

3. **iHARPERELLA**: Improved HARmonic (background) PhasE REmovaL using the LAplacian operator[18], included in STISuite Matlab toolbox provided by UC Berkeley (https://people.eecs.berkeley.edu/~chunlei.liu/software.html) and applied on Laplacian phase images obtained using 3D Laplacian phase unwrapping.

4. **VSHARP**: Sophisticated Harmonic Artifact Reduction for Phase data with varying spherical kernel[21], included in STISuite Matlab toolbox and applied on unwrapped phase images.

To acquire the final susceptibility maps, tissue phase images obtained using the above algorithms were further processed using iLSQR dipole inversion algorithm (see below) for comparison. For the multi-echo sequence performed on group 2 volunteers, background removal algorithms were applied on each echo individually. The resulting tissue phase images were then divided by their corresponding echo time and averaged to get a single tissue phase image for dipole inversion.

Phase-susceptibility Dipole Inversion—To compare the effects of different dipole inversion algorithms, four methods were selected, processed, and analyzed after performing background field removal with VSHARP. The regularization and threshold parameters for MEDI and CSC were individually optimized empirically by sweeping through a range of values and selecting the one that visually minimized both streaking artifacts and blurring.

1. **MEDI**: Morphology-Enabled Dipole Inversion[33], included in MEDI toolbox and required magnitude image, phase image and brain mask. We empirically determined that a regularization parameter of data fidelity of $\lambda = 500$ for group 1 and $\lambda = 2000$ for group 2 gave the best quality images with minimal streaking artifacts and blurring of structures.

2. **CSC**: Compressed Sensing Compensated QSM method[21], implemented in Matlab 2015b according to the published paper and required phase image and brain mask. We selected the k-space threshold as 0.0875, regularization parameters of the total variation term $\lambda_T = 0.001$ and the wavelet term $\lambda_W = 0.01$.

3. **iLSQR**: a method for estimating and removing streaking artifacts in QSM using improved LSQR algorithm[23], included in STISuite toolbox and required a phase image and brain mask.

4. **QSMGAN**: a deep learning convolutional neural network approach for QSM dipole inversion that was trained using 7T COSMOS QSM data and a 3D

Author Manuscript Author Manuscript Author Manuscript Author Manuscript

U-Net architecture with increased receptive field of the input phase compared to the output. A Wasserstein General Adversarial Network training strategy was employed[34].

Integrated QSM algorithm—We also included a QSM algorithm known as QSIP, or Quantitative Susceptibility mapping by Inversion of a Perturbation field model[28] that performs background removal and dipole inversion in an integrated way by updating the calculation of background field during dipole inversion. The code was developed in Matlab 2012b and provided by the author. For our analyses, we regarded QSIP as a dipole inversion method and compared it with the other four dipole inversion algorithms mentioned in the previous section.

COSMOS calculation—For the subjects in group 2, COSMOS QSM images[22] were calculated as the ground truth susceptibility map. Magnitude images acquired at 3 different head orientations were co-registered with FSL FLIRT[32] and the resulting transformations applied to the corresponding phase images from each orientation. The dipole field inversion was solved using the algorithm proposed by Liu et al., 2009[22] after background field removal with VSHARP.

Image Analysis

All the reconstructed QSM were zero-mean normalized by subtracting the mean susceptibility inside the brain mask before further analysis and comparison. The following 2 sections describe the metrics used for comparing techniques for each group. Figure 2 illustrates visually the definition of these quantified metrics used for comparison.

Group 1 (brain tumor patients with CMBs)

1. **Noise level and white matter homogeneity**.10 square ROIs of 150–250 voxels with relatively homogeneous susceptibility values in normal-appearing white matter were manually selected on each patient as in Figure 2A. Noise level was defined as the standard deviation of susceptibility values inside each ROI. White matter homogeneity was defined as the standard deviation of the mean susceptibility values of each ROI on each patient and is a proxy measure of residual background phase and low frequency artifacts.

2. **Vein contrast**. To measure the QSM reconstruction performance on veins, which have high susceptibility values due to the abundance of deoxyhemoglobin, we drew line profiles through transverse sections of veins on axial maximum intensity projected (8mm) susceptibility maps in order to quantify vein contrast as height divided by full width half height (FWHH) of the line profile (Figure 2B).

3. **Microbleed contrast**. Radiation-induced CMBs from each patient were segmented on reconstructed susceptibility weighted images (SWI) using in-house software[35,36]. Each resulting CMB mask was eroded by 1 voxel in the axial plane to remove the blooming artifact present on SWI. The periphery of a microbleed was calculated as the original mask subtracting the eroded

Author Manuscript Author Manuscript Author Manuscript Author Manuscript

mask. CMB contrast (C) was then calculated as the difference between mean susceptibilities of the CMB and its immediate periphery ($C = \chi_{\text{CMB}} - \chi_{\text{periphery}}$).

4. **Basal ganglia susceptibility**. Since QSM is commonly used to investigate iron deposition in deep gray matter, we compared the mean susceptibility of different QSM methods on the following five ROIs: red nucleus (RN), substantia nigra (SN), caudate nucleus (CN), putamen (PU), globus pallidus (GP). The ROIs were defined by warping a QSM atlas and its predefined whole brain segmentation[37] to individual COSMOS QSM using FSL non-linear registration tool FNIRL[32]. All ROI masks were visually assessed for accuracy after coregistration to the atlas and adjusted if necessary. Figure 3 shows example basal ganglia ROI segmentations fron a healthy volunteer.

Group 2 (healthy volunteers)

1. **Whole-brain susceptibility**. To numerically compare the QSM reconstruction accuracy of the whole brain, we adopted three metrics used in the 2016 QSM reconstruction challenge[38] described as follows:

   - **Root mean squared error (RMSE)**: Measures the relative residual error of the reconstructed QSM as:

     $$\text{RMSE} = 100 \times \frac{||\chi - \hat{\chi}||_2}{||\chi||_2}$$

     where χ represents the ground truth susceptibility map and $\hat{\chi}$ represents the reconstructed susceptibility map.

   - **High-frequency error norm (HFEN):** This metric described by Ravishankar and Bresler in 2011,[39] estimates the fidelity of reconstructed QSM at high spatial frequencies. It is computed by applying a LoG (Laplacian of a Gaussian) filter of the reconstructed and reference QSM volumes and calculating the L2 norm of their difference normalized by the norm of the filtered reference.

   - **Structural similarity index (SSIM)**: Described in Simoncelli et al., 2004,[40] this metric quantifies the “visual” similarity between the reconstructed QSM and the reference by combining three similarity components (luminance, contrast, structural).

2. **Basal ganglia ROI susceptibility**. Mean susceptibility values of different dipole inversion algorithms from basal ganglia ROIs using the same atlas-based approach as described for group 1, only with left and right ROIs measured separately, were compared to COSMOS. Linear regression was also conducted between different dipole inversion algorithms and COSMOS mapping using data from all basal ganglia ROIs together.

Author Manuscript Author Manuscript Author Manuscript Author Manuscript

Statistical methods

Kruskal-Wallis test and Wilcoxon signed rank tests were used to identify statistically significant differences pairwise among methods. Mann-Whitney (Wilcoxon rank-sum) tests were used to test for significant differences between samples of unequal sizes. A Bonferroni correction was adopted to reduce type I error (false positive results) from multiple comparisons.

Results

Noise level

Among the four background removal algorithms being compared, PDF had significantly higher noise levels than RESHARP at 3T and VSHARP at 7T ($p<0.01$; Figure 4A). At 3T, RESHARP also had significantly lower noise levels than iHARPERELLA ($p<0.01$). Among the five dipole inversion algorithms, QSMGAN and MEDI had significantly higher noise levels than the other three algorithms at 7T and both field strengths, respectively (Figure 4B). At 7T, iLSQR generated QSM images with the lowest noise ($p<0.05$), while at 3T QSMGAN had significantly lower noise than the other dipole inversion methods. Except for QSMGAN, all background field removal and dipole inversion algorithms achieved a lower noise level at 7T than 3T (all $p<0.01$), corresponding to the higher SNR available at 7T.

White matter homogeneity

At both field strengths, VSHARP and RESHARP had the highest white matter homogeneity (lowest standard deviation of mean susceptibility of the 10 ROIs within each patient) followed by PDF and iHARPERELLA (Figure 5A). Among the dipole inversion algorithms, iLSQR, QSIP, and QSMGAN had significantly improved white matter homogeneity compared to MEDI at 3T ($p<0.01$; Figure 5B), and increasing trends in white matter homogeneity were observed compared to CSC. Although similar trends were observed at 7T, QSIP and QSMGAN had the most homogenous images compared to the other techniques, with statistically significant increased homogeneity compared to both MEDI and CSC (all $p<0.01$). No statistically significant differences were observed between 3T and 7T for all background removal and dipole inversion algorithms.

Vein contrast

Figure 6 shows the boxplots of vein contrast of all evaluated methods. VSHARP provided higher vein contrast than all other three background removal algorithms at both field strengths ($p<0.05$). Of the five dipole inversion algorithms, QSMGAN provided significantly less vein contrast compared to all other algorithms ($p<0.0001$). iLSQR had higher vein contrast than CSC and MEDI at 3T, while QSIP exhibited improved vein contrast over MEDI ($p<0.001$ for iLSQR vs CSC, $p<0.01$ for iLSQR vs MEDI, $p=0.03$ for QSIP vs MEDI). At 7T, QSIP had higher vein contrast than all the other dipole inversion algorithms ($p<0.05$), with iLSQR also having significantly higher vein contrast than CSC ($p<0.001$). When algorithms were compared between field strengths, only QSMGAN had significantly elevated vein contrast at 7T compared to 3T ($p<0.01$). Figure 7 provides a visual comparison of a vein processed by different algorithms at both field strengths. Note that the images at

Author Manuscript Author Manuscript Author Manuscript Author Manuscript

3T and 7T were not coregistered in order to avoid alterations in image quality caused by interpolation during alignment, so the orientation of the vein varies slightly between field strengths.

CMB Contrast

No significant differences were observed in CMB contrast among all of the background field removal algorithms (Kruskal-Wallis p=0.52 and 0.22 for 3T and 7T respectively, boxplots in Figure 8A). Among the dipole inversion algorithms, QSIP had significantly higher CMB contrast than other methods at both field strengths, while QSMGAN had significantly lower CMB contrast ($p < 0.0001$, Figure 8B). Only QSMGAN showed a statistically significant difference between field strengths. Figure 9 demonstrates a visual comparison of three CMBs computed using different background field removal algorithms at 3T and 7T. Similar to the measurement and display of vein contrast, the orientations of CMBs shown in Figure 9 are displayed without co-registration between field strengths.

Basal Ganglia ROIs

Figures 10 and 11 show boxplots of mean susceptibilities within different basal ganglia ROIs for the different background field removal (Figure 10) and dipole inversion (Figure 11) algorithms in patients with radiation-induce CMBs. At 7T, no significant differences were found in susceptibility values among background field removal methods in any basal ganglia ROI, though values tended to be reduced in the substantia nigra and red nucleus with PDF (Figure 10). At 3T, more variability was observed among methods, especially substantia nigra and red nucleus (Figure 10). The p-values that were less than 0.001 for differences among the background field removal and dipole inversion methods for each region are dispayed in Tables 2 and 3, respectively, where asterisks indicate statistical significance after multiple comparison correction. At 3T, QSMGAN resulted in significantly lower susceptibility values compared to all other methods in all regions except for when compared to QSIP in the caudate and putamen where QSIP was also significantly reduced compared to other methods. In the globus pallidus and substantia nigra MEDI resulted in significantly elevated susceptibility values compared to all other methods. Although no significant differences were found among any methods in any region at 7T after correcting for multiple comparisons, similar trends were observed in all regions where QSMGAN had the lowest mean susceptibility compared to the other methods, while values quantified using MEDI were the highest (Figure 11). No significant differences were observed between field strengths.

Figure 12 shows the boxplot of mean susceptibilities within different basal ganglia ROIs for the different dipole inversion algorithms in the 8 volunteers scanned with 3 head orientations to compare against COSMOS as a gold standard. All algorithms except QSMGAN overestimated susceptibility in the left substantia nigra and underestimated susceptibility values in the caudate nucleus and putamen, especially QSIP. In the globus palidus, all methods underestimated susceptibility compared to COSMOS. Figure 13 row 1 shows an axial slice of the striatum confirming these findings. Figure 14 displays scatter plots of susceptibility values within each ROI for each dipole inversion algorithm compared to COSMOS. The ideal algorithm would achieve a regression line close to identity with low

Author Manuscript Author Manuscript Author Manuscript Author Manuscript

residual error (or a coefficient of determination R close to 1). As expected, susceptibility values quantified with QSMGAN were the most correlated with those attained using COSMOS, although its slope deviated from 1 at higher values of susceptibility. iLSQR achieved a slope closest to 1 and the 2nd highest correlation coefficient, while QSIP had a more dispersed scatter plot and lower R^2 than the other four algorithms. However, because COSMOS used the same VSHARP algorithm for background field removal as iLSQR, CSC, and MEDI while QSIP integrated background removal into its processing, the lower performance might in part be explained by differences in background field removal rather than dipole inversion approaches.

Whole-brain QSM metrics

RMSE, HFEN, and SSIM of the five dipole inversion algorithms compared to COSMOS are listed in Table 4. QSMGAN followed by iLSQR had significantly lower RMSE and HFEN compared to other methods ($p < 0.01$). For HFEN, QSMGAN, iLSQR and QSIP were significantly reduced compared to CSC and MEDI ($p < 0.01$), indicating less deviation from COSMOS for these algorithms. MEDI achieved the highest SSIM to COSMOS among all the dipole inversion algorithms ($p < 0.01$), followed by QSIP and iLSQR. Figure 13 visually compares all the dipole inversion algorithms against COSMOS QSM (with VSHARP for background field removal). Although all algorithms achieved relatively low to no residual streaking artifacts, they have distinct appearances due to different regularization approaches.

Discussion

The results of this study highlight the importance of carefully selecting a QSM processing strategy based on the anatomy and question of interest. Susceptibility values can vary based on the method selected for both background field removal and dipole inversion and different strategies may be more optimal depending on the question of interest. Our results suggest that for the visualization of smaller vascular structures or an analysis that takes on a more global whole brain approach, an integrated method such as QSIP would be advantageous. On the other hand, if accurate quantification of susceptibility or iron deposition within larger structures such as those comprising the striatum is the goal, our results favor VSHARP + iLSQR as the methods of choice.

To simplify the comparison process, we selected iLSQR for all background field removal methods and VSHARP for all dipole inversion methods, except for QSIP, which is an integrated algorithm. These two methods were selected as base algorithms for three main reasons: 1) better visual quality of reconstructed QSM 2) better performance in many numerical metrics we compared, and 3) relatively high computational efficiency as shown in Table 1. Two different groups of subjects were scanned with different parameters in this study in order to cover the majority of use cases of QSM. Group 1 was comprised of brain tumor patients who developed radiation-induced CMBs, an ideal example of abnormal susceptibility. This group of patients were scanned with higher axial-plane resolution sequence to maximize the detection ability of small brain lesions and cerebrovascular structures such as veins. Group 2, on the other hand, consisted of healthy volunteers that were scanned using a multi-echo sequence with isotropic resolution designed for

Author Manuscript Author Manuscript Author Manuscript Author Manuscript

the investigation of iron deposition within the basal ganglia, where research of most neurodegenerative diseases involving QSM have been heavily studied. As the high in-plane spatial resolution was not as critical as in patients with CMBs, we could reduce the axial-plane resolution to match the z-direction resolution to achieve an isotropic configuration. This isotropic setting could also facilitate the processing of COSMOS QSM, which requires the co-registration of scans conducted at different head orientations.

In patients with CMBs, we observed that QSM at 7T has a lower noise level than at 3T. Besides the intrinsic benefit of higher signal-to-noise ratio inherent with increasing field strength, the sequence used at 7T could have potentially induced more phase accumulation than that employed at 3T ($\gamma \times B_0 \times TE = 4.77\ ppm$ at 7T vs. $\gamma \times B_0 \times TE = 3.58\ ppm$ at 3T). In this study, we defined a metric called white matter homogeneity by calculating the standard deviation of mean susceptibility measured in ten different square ROIs drawn on pure white matter under the assumption that the resulting QSM of white matter should be relatively homogeneous if the processing pipeline is robust. A high standard deviation or low homogeneity likely indicates either more residual background phase components or other low spatial frequency artifacts. MEDI resulted in the most inhomogeneous susceptibility maps at both field strengths, which was reflected by both the large variations between different white matter ROIs in the same patient and higher noise levels, despite the concomitant regional blurring common with this method. This discrepancy could possibly be explained by inconsistent boundaries between the magnitude images and the susceptibility map or the fact that it is more sensitive to the regularization parameter which was optimized empirically for our dataset. The increased noise observed in QSMGAN images could be due to the fact that the network was trained on a higher SNR dataset with larger voxel sizes than what was acquired on the patients. The fact that QSIP and QSMGAN images were the most homogeneous regardless of field strength, suggests that imperfect background field removal may be a contributor to the inhomogeneity present in the other dipole inversion methods and supports the benefits of using deep learning and an integrated approach to overcome this limitation.

The rationale for comparing vein and CMB contrast among algorithms was to 1) examine the residual low spatial frequency artifacts, and 2) validate the algorithms on tissue and lesions with relatively high susceptibility values. QSIP produced the highest vein and CMB contrast at both field strengths and may be the optimal method for applications requiring the segmentation of these structures, whereas QSMGAN performed the worse likely because it was trained on data obtained from healty volunteers. The lower vein contrast of MEDI might be due to 1) higher brain tissue susceptibility and 2) blurrier vein structure caused by regularization. Although we favored higher contrast in this comparison, our results cannot be translated to higher accuracy of reconstructed QSM because ground truth susceptibility maps or COSMOS scans were not obtained.

Although QSIP outperformed the other dipole inversion algorithms on the majority of metrics, it resulted in values that were the most different from the gold standard COSMOS images likely because all the other methods (including COSMOS) all first applied VSHARP for background field removal. This was demonstrated by susceptibility values within the striatal regions being significantly lower than those derived from COSMOS, as well as

Author Manuscript Author Manuscript Author Manuscript Author Manuscript

weaker correlation coefficients observed across all regions. More inferiorly in the substantia nigra and red nuclei, however, QSIP resulted in susceptibility values that were the most similar to those quantified by COSMOS while QSMGAN showed the greatest deviation from COSMOS values in these regions with higher susceptibility values. Although overall QSMGAN unsurprisingly resulted in the highest correlation with COSMOS because that is what it was trained on, iLSQR, on the other hand, consistently resulted in the most similar susceptibility values to COSMOS across all basal ganglia analyses, making it the preferred method for local absolute quantification of susceptibility within smaller structures.

There are several additional limitations of this study. First, we chose to compare methods that are most widely utilized in the literature for neurological applications and were accessible, realizing that this approach is biased against newer, potentially improved methodologies. Although we conducted a relatively coarse grid-search of parameters and empirically selected the ones that achieved the best visual correspondence with the other algorithms, we did not compare how varying regularization and other parameters affected the quantification of our comparison metrics, especially for methods such as CSC and MEDI that are more sensitive to parameter tuning. It is also possible that further fine-tuning and optimization of these methods may achieve improved QSM reconstruction. Since some of our comparison metrics such as noise level and homogeneity are a direct consequence of spatial filtering, they would be the most affected by variations due to parameter selection. The complete processing pipeline of QSM consists of other pre-processing steps before background field removal, such as multi-coil phase combination and phase unwrapping, that could also affect the resulting QSM image quality and quantification accuracy[41] were not investigated in this paper. Similarly, in order to compare data among different patients, we performed zero-mean normalization, which may introduce a bias in the quantification of RMSE and basal ganglia susceptibility. For our group of healthy volunteers, we chose COSMOS as the ground truth susceptibility map for comparison and in our patients we used white matter homogeneity as a quality metric for comparison. Thes methods, however, ignore the susceptibility anisotropy present in myelin and white matter fiber tracts. Although Langkammer et al[38] have suggested using the last diagonal component (χ_{33}) in susceptibility tensor theory[42], our data acquisition scheme was limited to three orientations, making the calculation of χ_{33} impossible. But because basal ganglia susceptibility is relatively isotropic, COSMOS should still be a valid image of ground truth of susceptibility in our striatal ROI analyses. Future studies could perform a data acquisition that enables the reconstruction of χ_{33} and use it as the ground truth for comparison on other brain tissue with higher susceptibility anisotropy for a more accurate comparison of RMSE, HFEN, and SSIM which can be biased by white matter anisotropy. Since QSM is recently gaining traction in other organs such as liver and kidney, a similar evaluation should be performed in these organs.

In conclusion, this work evaluated and compared a variety of commonly adopted algorithms for background field removal and dipole inversion of QSM. When applied to patients with CMBs scanned at both 3T and 7T, we found that 7T MRI could provide QSM images with lower noise than 3T MRI. QSIP and VSHARP + iLSQR achieved the highest white matter homogeneity and vein contrast, with QSIP also providing the highest CMB contrast. Compared to ground truth COSMOS QSM images, iLSQR and QSIP had the lowest RMSE

Author Manuscript Author Manuscript Author Manuscript Author Manuscript

and HFEN, while MEDI achieved best SSIM. Although variations were observed among methods throughout the entire brain, overall good correlations between susceptibility values of dipole inversion algorithms and the COSMOS reference were observed in the basal ganglia ROIs, with VSHARP + iLSQR achieving the most similar susceptibility values to COSMOS. This work suggests that selection of QSM method can not only influence the quality of maps obtained but could potentially affect the quantification of iron or CMB detection in studies that rely on precise quantification of a spatial distribution of susceptibility values.

Acknowledgements

Funding:

This work was supported by NIH NINDS grant R01NS099564 and GE Healthcare

Abbreviations:

MRI	Magnetic Resonance Imaging
QSM	Quantitative Susceptibility Mapping
CMB	Cerebral Microbleed
SN	Substantia Nigra
RN	Red Nucleus
GP	Globus Pallidus
PN	Putamen Nucleus
CN	Caudate Nucleus

References

1. Langkammer C, Schweser F, Shmueli K, Kames C, Li X, Guo L, Kim J, Wei H, Bredies K, Buch S, Guo Y, Liu Z, Rauscher A, Bilgic B, Sciences B, Sciences B, Science R, Sciences C, Computing S, Quantitative Susceptibility Mapping: Report from the 2016 Reconstruction Challenge. 2016.
2. Li W, Wu B, Liu C. Quantitative susceptibility mapping of human brain reflects spatial variation in tissue composition. Neuroimage 2011;55:1645–1656. [PubMed: 21224002]
3. Sun H, Klahr AC, Kate M, Gioia LC, Emery DJ, Butcher KS, Wilman AH. Quantitative susceptibility mapping for following intracranial hemorrhage. Radiology 2018;288:830–839. [PubMed: 29916778]
4. Vaas M, Deistung A, Reichenbach JR, Keller A, Kipar A, Klohs J. Vascular and Tissue Changes of Magnetic Susceptibility in the Mouse Brain After Transient Cerebral Ischemia. Transl. Stroke Res 2018;9:426–435. [PubMed: 29177950]
5. Zivadinov R, Tavazzi E, Bergsland N, Hagemeier J, Lin F, Dwyer MG, Carl E, Kolb C, Hojnacki D, Ramasamy D, Durfee J, Weinstock-Guttman B, Schweser F. Brain iron at quantitative MRI is associated with disability in multiple sclerosis. Radiology 2018;289:487–496. [PubMed: 30015589]
6. He N, Ling H, Ding B, Huang J, Zhang Y, Zhang Z, Liu C, Chen K, Yan F. Region-specific disturbed iron distribution in early idiopathic Parkinson's disease measured by quantitative susceptibility mapping. Hum. Brain Mapp 2015;36:4407–4420. [PubMed: 26249218]

Author Manuscript Author Manuscript Author Manuscript Author Manuscript

7. Acosta-Cabronero J, Williams GB, Cardenas-Blanco A, Arnold RJ, Lupson V, Nestor PJ. In vivo quantitative susceptibility mapping (QSM) in Alzheimer's disease. PLoS One 8. 2013 Nov 21;8(11):e81093.
8. Van Bergen JMG, Hua J, Unschuld PG, Lim IAL, Jones CK, Margolis RL, Ross CA, Van Zijl PCM, Li X. Quantitative susceptibility mapping suggests altered brain iron in premanifest Huntington disease. Am. J. Neuroradiol 2016;37:789–796. [PubMed: 26680466]
9. Schweitzer AD, Liu T, Gupta A, Zheng K, Seedial S, Shtilbans A, Shahbazi M, Lange D, Wang Y, Tsiouris AJ. Quantitative susceptibility mapping of the motor cortex in amyotrophic lateral sclerosis and primary lateral sclerosis. Am. J. Roentgenol 2015;204:1086–1092. [PubMed: 25905946]
10. Lupo JM, Chuang CF, Chang SM, Barani IJ, Jimenez B, Hess CP, Nelson SJ. 7-Tesla susceptibility-weighted imaging to assess the effects of radiotherapy on normal-appearing brain in patients with glioma. Int J Radiat Oncol Biol Phys 2012 Mar 1;82(3):e493–500. [PubMed: 22000750]
11. Lupo JM, Molinaro AM, Essock-Burns E, Butowski N, Chang SM, Cha S, Nelson SJ. The effects of anti-angiogenic therapy on the formation of radiation-induced microbleeds in normal brain tissue of patients with glioma. Neuro. Oncol 2016;18:87–95. [PubMed: 26206774]
12. Yates PA, Villemagne VL, Ellis KA, Desmond PM, Masters CL, Rowe CC. Cerebral microbleeds: A review of clinical, genetic, and neuroimaging associations. Front. Neurol 2014 Jan 6;4:205. [PubMed: 24432010]
13. Charidimou A, Krishnan A, Werring DJ, Rolf Jäger H. Cerebral microbleeds: A guide to detection and clinical relevance in different disease settings. Neuroradiology 2013;55;655–674. [PubMed: 23708941]
14. Liu T, Surapaneni K, Lou M, Cheng L, Spincemaille P, Wang Y. Cerebral microbleeds: burden assessment by using quantitative susceptibility mapping. Radiology 2012;262:269–78. [PubMed: 22056688]
15. Zecca L, Youdim MBH, Riederer P, Connor JR, Crichton RR. Iron, brain ageing and neurodegenerative disorders. Nat. Rev. Neurosci 2004;5:863–873. [PubMed: 15496864]
16. Wang Y, Spincemaille P, Liu Z, Dimov A, Deh K, Li J, Zhang Y, Yao Y, Gillen KM, Wilman AH, Gupta A, Tsiouris AJ, Kovanlikaya I, Chiang GCY, Weinsaft JW, Tanenbaum L, Chen W, Zhu W, Chang S, Lou M, Kopell BH, Kaplitt MG, Devos D, Hirai T, Huang X, Korogi Y, Shtilbans A, Jahng GH, Pelletier D, Gauthier SA, Pitt D, Bush AI, Brittenham GM, Prince MR. Clinical quantitative susceptibility mapping (QSM): Biometal imaging and its emerging roles in patient care. J. Magn. Reson. Imaging 2017 Oct;46(4):951–971. [PubMed: 28295954]
17. Liu C, Li W, Tong K, Yeom KW, Kuzminski S. Susceptibility-weighted imaging and quantitative susceptibility mapping in the brain. J. Magn. Reson. Imaging 2015;42:23–41. [PubMed: 25270052]
18. Li W, Wu B, Liu C. iHARPERELLA: an improved method for integrated 3D phase unwrapping and background phase removal. Proc. Intl. Soc. Mag. Reson. Med 2015;23:3313.
19. Liu T, Khalidov I, De Rochefort L, Spincemaille P. A novel background field removal method for MRI using projection onto dipole fields (PDF). NMR Biomed. 2011 Nov;24(9):1129–1136. [PubMed: 21387445]
20. Sun H, Wilman AH. Background field removal using spherical mean value filtering and Tikhonov regularization. Magn. Reson. Med 2014;71:1151–1157. [PubMed: 23666788]
21. Wu B, Li W, Guidon A, Liu C. Whole brain susceptibility mapping using compressed sensing. Magn. Reson. Med 2012;67:137–147. [PubMed: 21671269]
22. Liu T, Spincemaille P, De Rochefort L, Kressler B, Wang Y. Calculation of susceptibility through multiple orientation sampling (COSMOS): a method for conditioning the inverse problem from measured magnetic field map to susceptibility source image MRI. Magn. Reson. Med 2009 Jan;61(1):196–204. [PubMed: 19097205]
23. Li W, Wang N, Yu F, Han H, Cao W, Romero R, Tantiwongkosi B, Duong TQ, Liu C, A method for estimating and removing streaking artifacts in quantitative susceptibility mapping. Neuroimage 2015;108:111–122. [PubMed: 25536496]

Author Manuscript Author Manuscript Author Manuscript Author Manuscript

24. Chen Y, Jakary A, Avadiappan S, Hess CP, Lupo JM. QSMGAN: Improved Quantitative Susceptibility Mapping using 3D Generative Adversarial Networks with increased receptive field. Neuroimage. 2020 Feb 15;207:116389.
25. Liu J, Liu T, De Rochefort L, Ledoux J, Khalidov I, Chen W, Tsiouris AJ, Wisnieff C, Spincemaille P, Prince MR, Wang Y. Morphology enabled dipole inversion for quantitative susceptibility mapping using structural consistency between the magnitude image and the susceptibility map. Neuroimage 2012;59:2560–2568. [PubMed: 21925276]
26. Yoon J, Gong E, Chatnuntawech I, Bilgic B, Lee J, Jung W, Ko J, Jung H, Setsompop K, Zaharchuk G, Kim EY, Pauly J, Lee J. Quantitative susceptibility mapping using deep neural network: QSMnet. Neuroimage 2018;179:199–206. [PubMed: 29894829]
27. Chen Y, Jakary A, Avadiappan S, Hess CP, Lupo JM. QSMGAN: Improved Quantitative Susceptibility Mapping using 3D Generative Adversarial Networks with increased receptive field. Neuroimage. 2020 Feb 15;207: 116389.
28. Chatnuntawech I, Mcdaniel P, Cauley SF, Gagoski BA, Langkammer C, Martin A, Grant PE, Wald LL, Setsompop K, Adalsteinsson E, Bilgic B. Single-step quantitative susceptibility mapping with variational penalties. NMR Biomed 2017 Apr;30(4):3570.
29. Poynton C, Jankinson M, Adalsteinsson E, Sullivan E, Pfefferbaum A, Wells W. Quantitative Susceptibility Mapping by Inversion of a Perturbation Field Model: Correlation with Brain Iron in Normal Aging. IEEE Trans. Med. Imaging 2015;34:339–353. [PubMed: 25248179]
30. Lupo JM, Banerjee S, Hammond KE, Kelley DA, Xu D, Chang SM, Vigneron DB, Majumdar S, Nelson SJ. GRAPPA-based susceptibility-weighted imaging of normal volunteers and patients with brain tumor at 7 T. Magn Reson Imaging. 2009 May;27(4):480–8. [PubMed: 18823730]
31. Beatty PJ, Brau AC, Chang S, Joshi SM, Michelich CR, Bayram E, Nelson TE, Herfkens RJ, Brittain JH. A method for autocalibrating 2-D accelerated volumetric parallel imaging with clinically practical reconstruction times, in: Proceedings of the International Society for Magnetic Resonance in Medicine 2007;15:1749.
32. Eckstein K, Dymerska B, Bachrata B, Bogner W, Poljanc K, Trattnig S, Robinson SD. Computationally Efficient Combination of Multi-channel Phase Data From Multi-echo Acquisitions (ASPIRE). Magn. Reson. Med 2017;c:1–11.
33. Jenkinson M, Beckmann CF, Behrens TEJ, Woolrich MW, Smith SM. FSL. Neuroimage 2012;62: 782–790. [PubMed: 21979382]
34. Liu T, Liu J, De Rochefort L, Spincemaille P, Khalidov I, Ledoux JR, Wang Y. Morphology enabled dipole inversion (MEDI) from a single-angle acquisition: Comparison with COSMOS in human brain imaging. Magn. Reson. Med 2011;66:777–783. [PubMed: 21465541]
35. Chen Y, Villanueva-Meyer JE, Morrison MA, Lupo JM. Toward Automatic Detection of Radiation-Induced Cerebral Microbleeds Using a 3D Deep Residual Network. J. Digit. Imaging 2019 Oct;32(5):766–772. [PubMed: 30511280]
36. Morrison MA, Payabvash S, Chen Y, Avadiappan S, Shah M, Zou X, Hess CP, Lupo JM. A user-guided tool for semi-automated cerebral microbleed detection and volume segmentation: Evaluating vascular injury and data labelling for machine learning. NeuroImage Clin. , 2018;20:498–505. [PubMed: 30140608]
37. Zhang Y, Wei H, Cronin MJ, He N, Yan F, Liu C. Longitudinal atlas for normative human brain development and aging over the lifespan using quantitative susceptibility mapping. Neuroimage 2018;171:176–189. [PubMed: 29325780]
38. Langkammer C, Schweser F, Shmueli K, Kames C, Li X, Guo L, Milovic C, Kim J, Wei H, Bredies K, Buch S, Guo Y, Liu Z, Meineke J, Rauscher A, Marques JP, Bilgic B. Quantitative susceptibility mapping: Report from the 2016 reconstruction challenge. Magn. Reson. Med 2018;79:1661–1673. [PubMed: 28762243]
39. Ravishankar S, Bresler Y. MR image reconstruction from highly undersampled k-space data by dictionary learning. IEEE Trans. Med. Imaging 2011;30:1028–1041. [PubMed: 21047708]
40. Simoncelli EP, Sheikh HR, Bovik AC, Wang Z. Image quality assessment: From error visibility to structural similarity. IEEE Trans. image Process 2004;13:600–612. [PubMed: 15376593]

Author Manuscript Author Manuscript Author Manuscript Author Manuscript

41. Cronin MJ, Wang N, Decker KS, Wei H, Zhu WZ, Liu C. Exploring the origins of TE-dependent QSM measurements in healthy tissue and cerebral microbleeds. Neuroimage 2017;149:98–113. [PubMed: 28126551]

42. Liu C.Susceptibility tensor imaging. Magn. Reson. Med 2010;63:1471–1477. [PubMed: 20512849]

Author Manuscript Author Manuscript Author Manuscript Author Manuscript

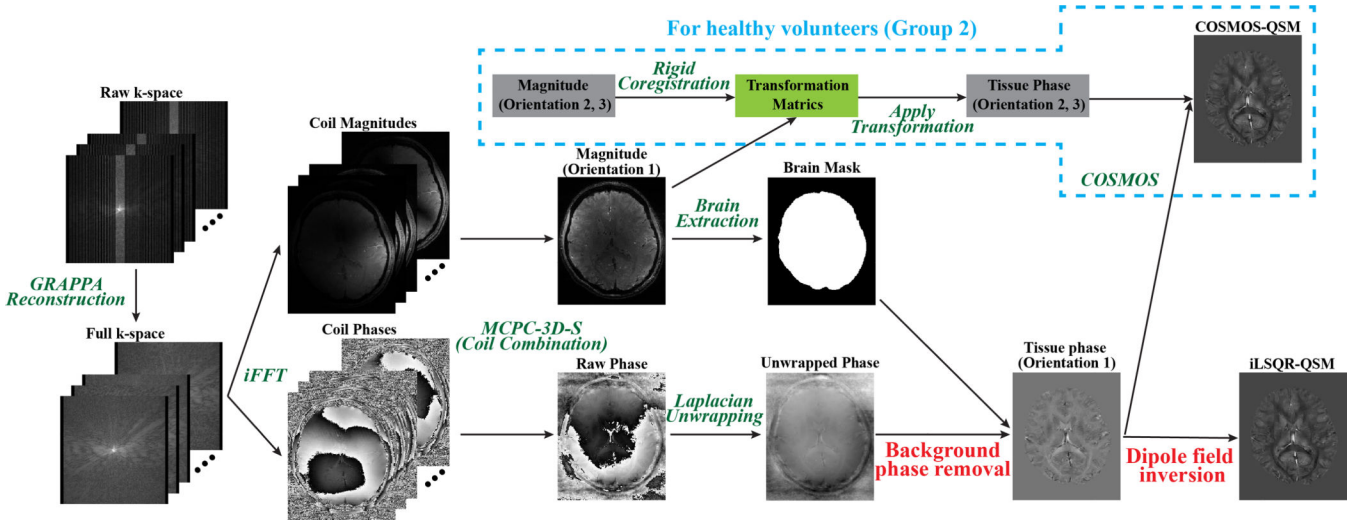

Figure 1.

QSM processing pipeline. Blue dashed box only applied on group 2 subjects with multiple orientation scans to reconstruct COSMOS QSM.

Author Manuscript

Author Manuscript

Author Manuscript

Author Manuscript

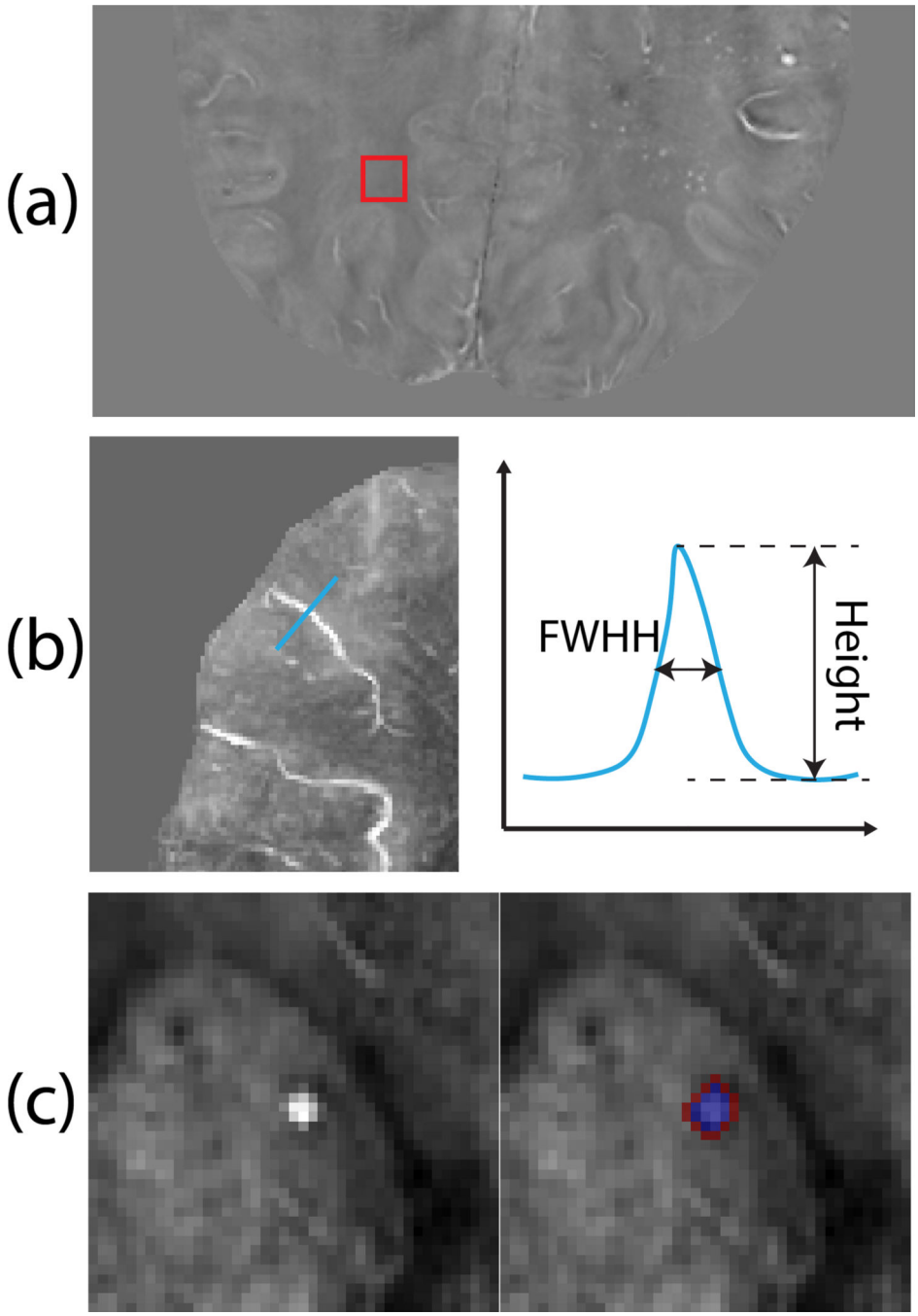

Figure 2.

Definition of metrics used for brain tumor patients with radiation-induced microbleeds. (a) An example square ROI drawn on white matter to measure noise level and white matter homogeneity. (b) An example line profile perpendicular to a vein on maximum intensity projected QSM and the definition of line profile height and FWHH is shown on the right. (c) Left: a CMB on iLSQR-VSHARP QSM. Right: blue area defines the CMB mask and the red area defines its peripheral region.

Author Manuscript Author Manuscript Author Manuscript Author Manuscript

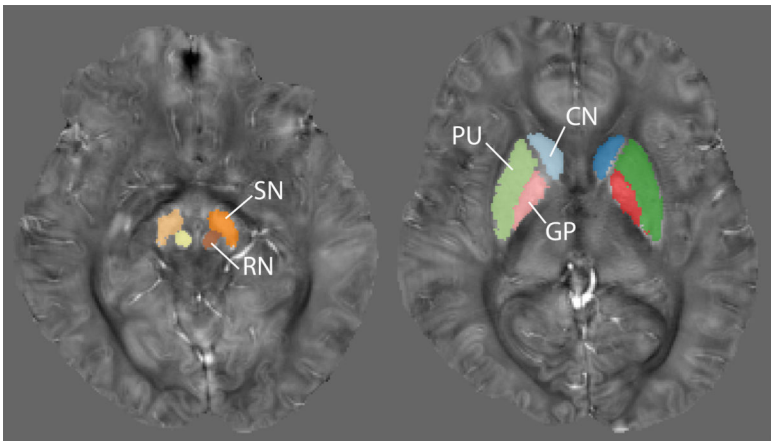

Figure 3.
Segmenation of basal ganglia ROIs for an example healthy volunteer after applying the QSM atlas. ROI names were labeled on the image.

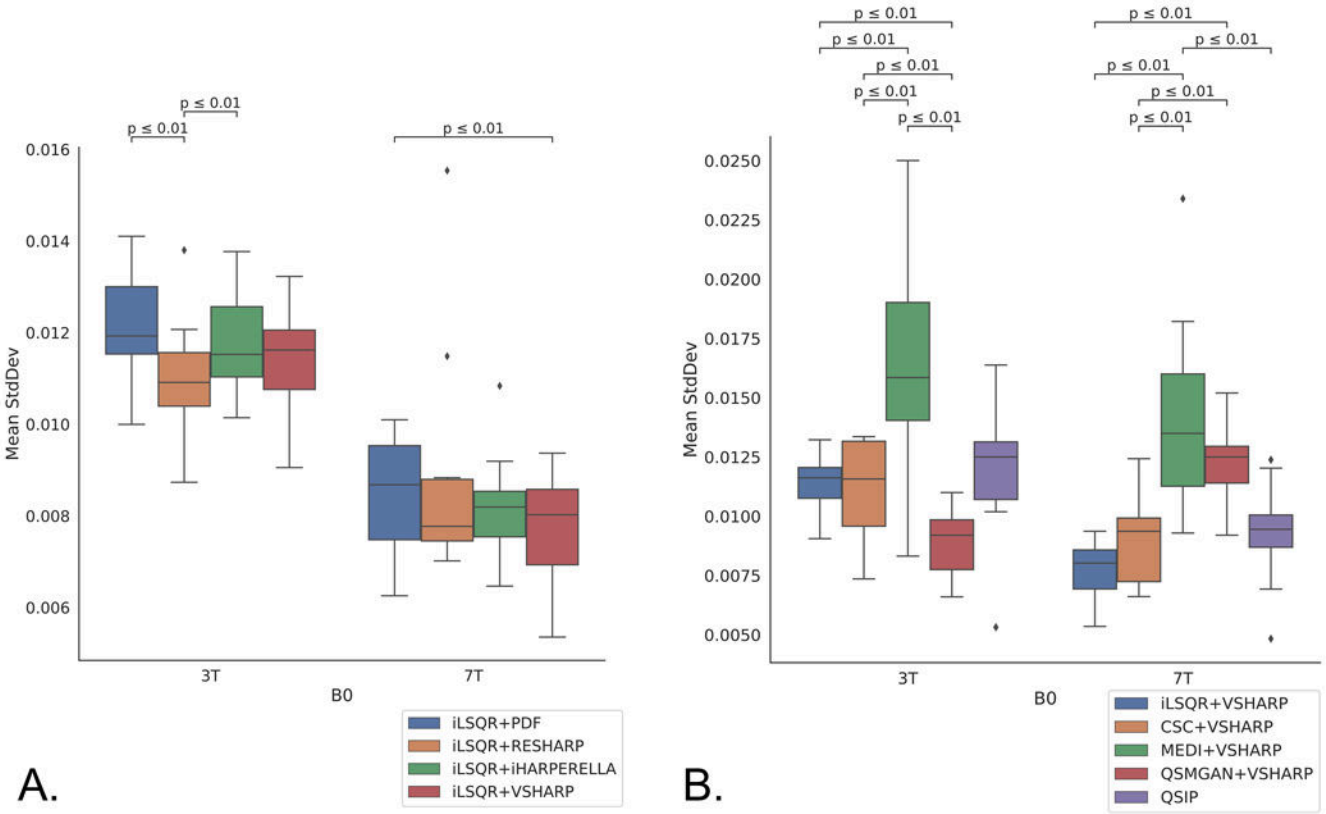

Figure 4.

Boxplots of noise levels at 3T and 7T as quantified by the mean standard deviation of 10 white matter ROIs for each patient. (A) Comparison among background field removal algorithms. (B) Comparison among dipole inversion methods. Lower error bars are the 25th percentile - 1.5 * interquartile range (IQR) or the mimumum value if it is larger, while upper error bars reflect the 75th percentile + 1.5 * IQR or maximum value if it is smaller.

Author Manuscript
Author Manuscript
Author Manuscript
Author Manuscript

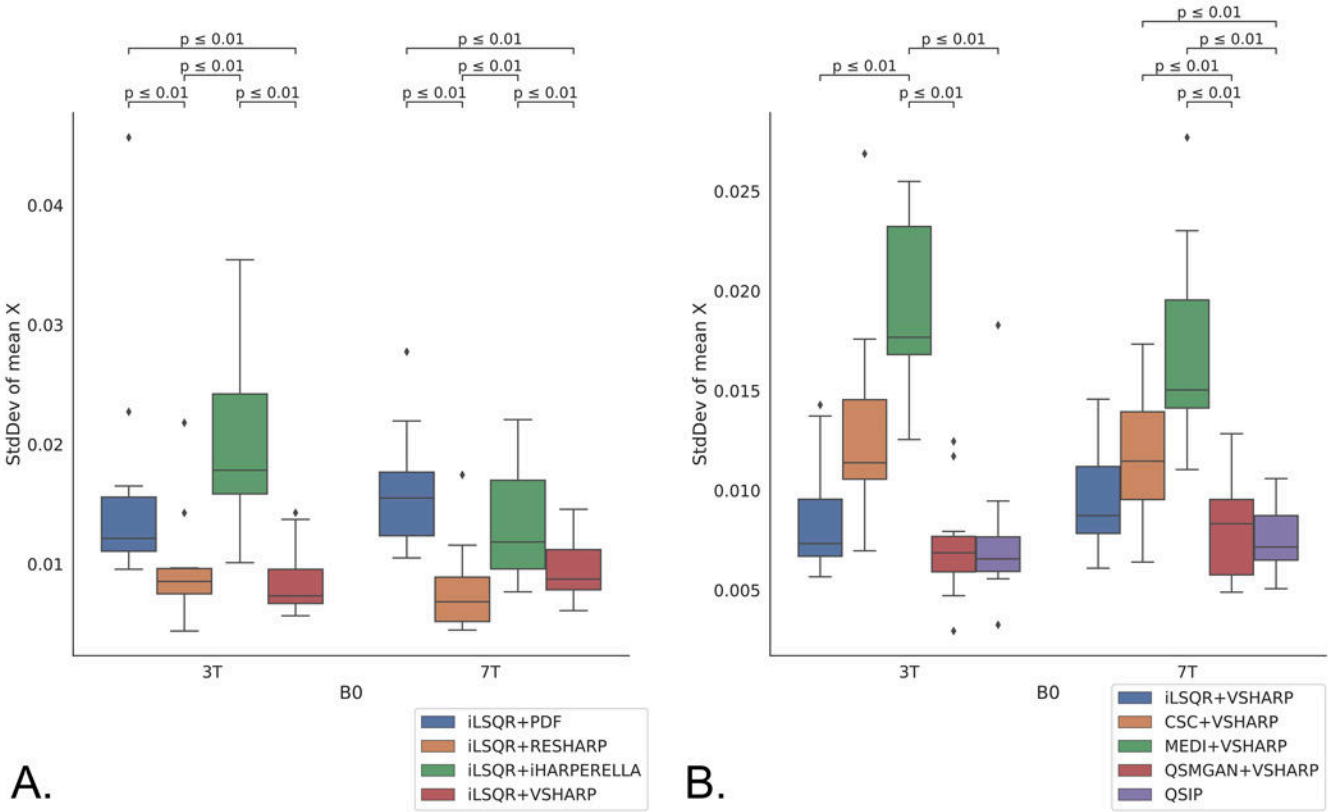

Figure 5.

Boxplots of white matter homogeneity at 3T and 7T as quantified by the standard deviation of the mean value from 10 white matter ROIs for each patient. (A) Comparison among background field removal algorithms. (B) Comparison among dipole inversion methods. Lower error bars are the 25th percentile - 1.5 * IQR or the mimumum value if it is larger, while upper error bars reflect the 75th percentile + 1.5 * IQR or maximum value if it is smaller.

Author Manuscript
Author Manuscript
Author Manuscript
Author Manuscript

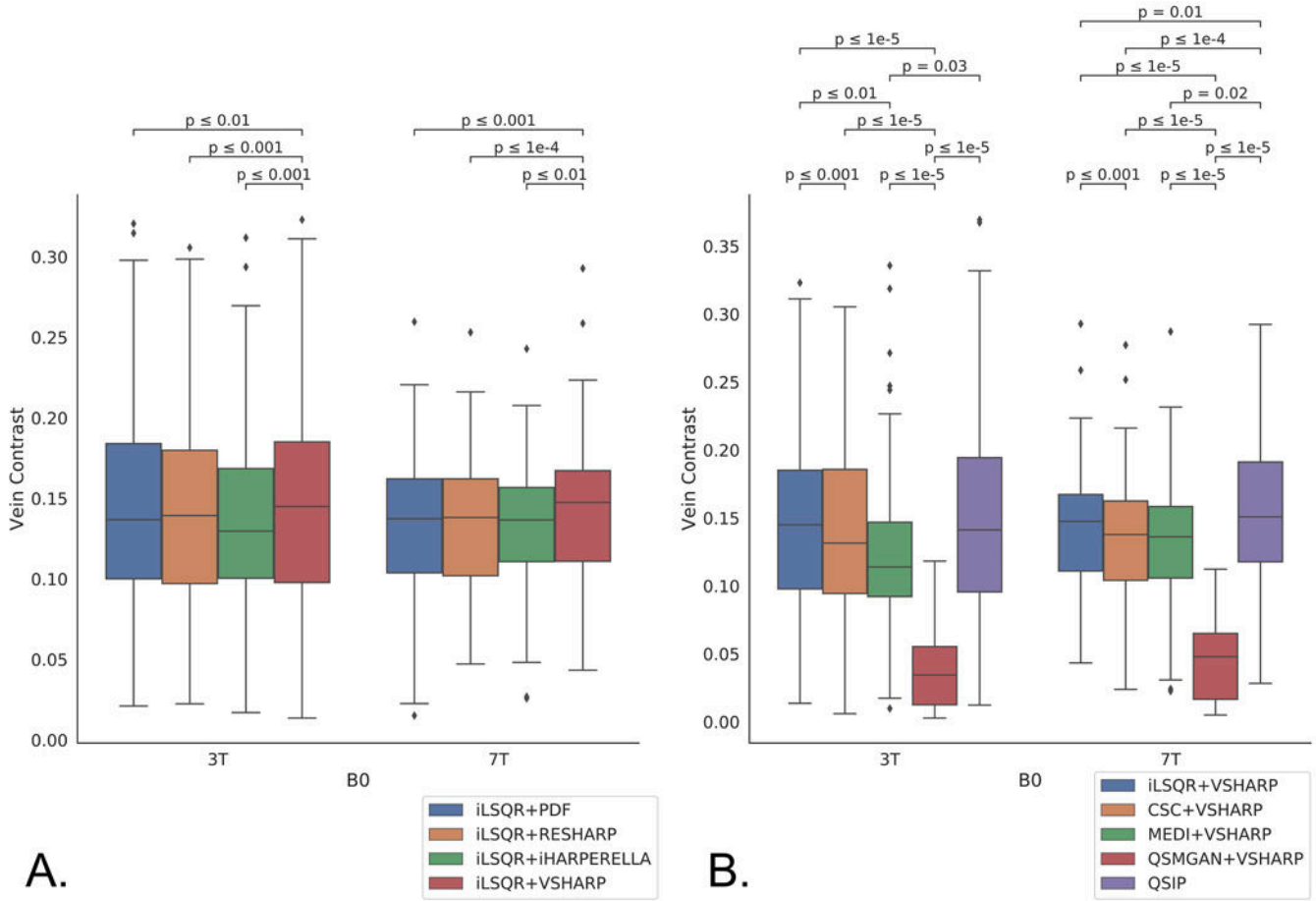

Figure 6.

Boxplots of vein contrast quantified from line profile analysis at 3T and 7T. (A) Comparison among background field removal algorithms. (B) Comparison among dipole inversion methods. Lower error bars are the 25th percentile - 1.5 * IQR or the mimumum value if it is larger, while upper error bars reflect the 75th percentile + 1.5 * IQR or maximum value if it is smaller.

Author Manuscript
Author Manuscript
Author Manuscript
Author Manuscript

Author Manuscript Author Manuscript Author Manuscript Author Manuscript

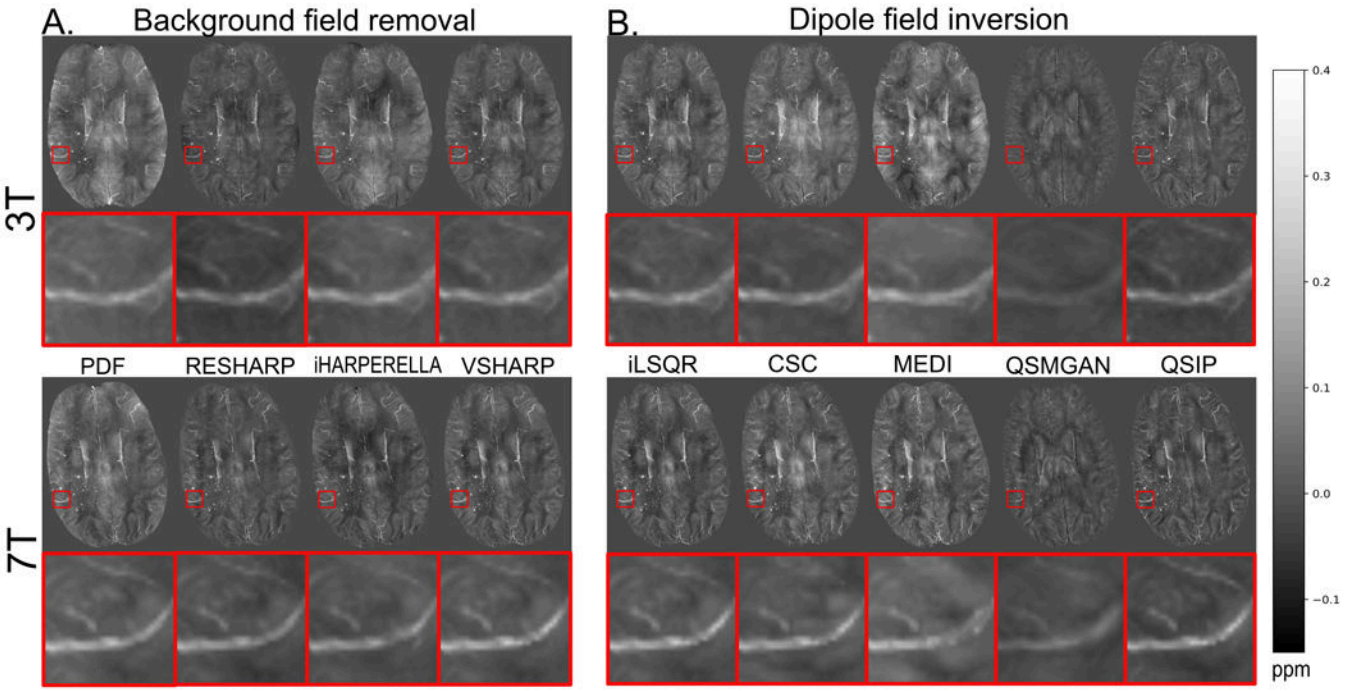

Figure 7.

Visual comparison of vein contrast from different algorithms at 3T and 7T. Top left: background field removal algorithms at 3T. Top right: dipole inversion algorithms at 3T. Bottom left: background field removal algorithms at 7T. Bottom right: dipole inversion algorithms at 7T.

Author Manuscript

Author Manuscript

Author Manuscript

Author Manuscript

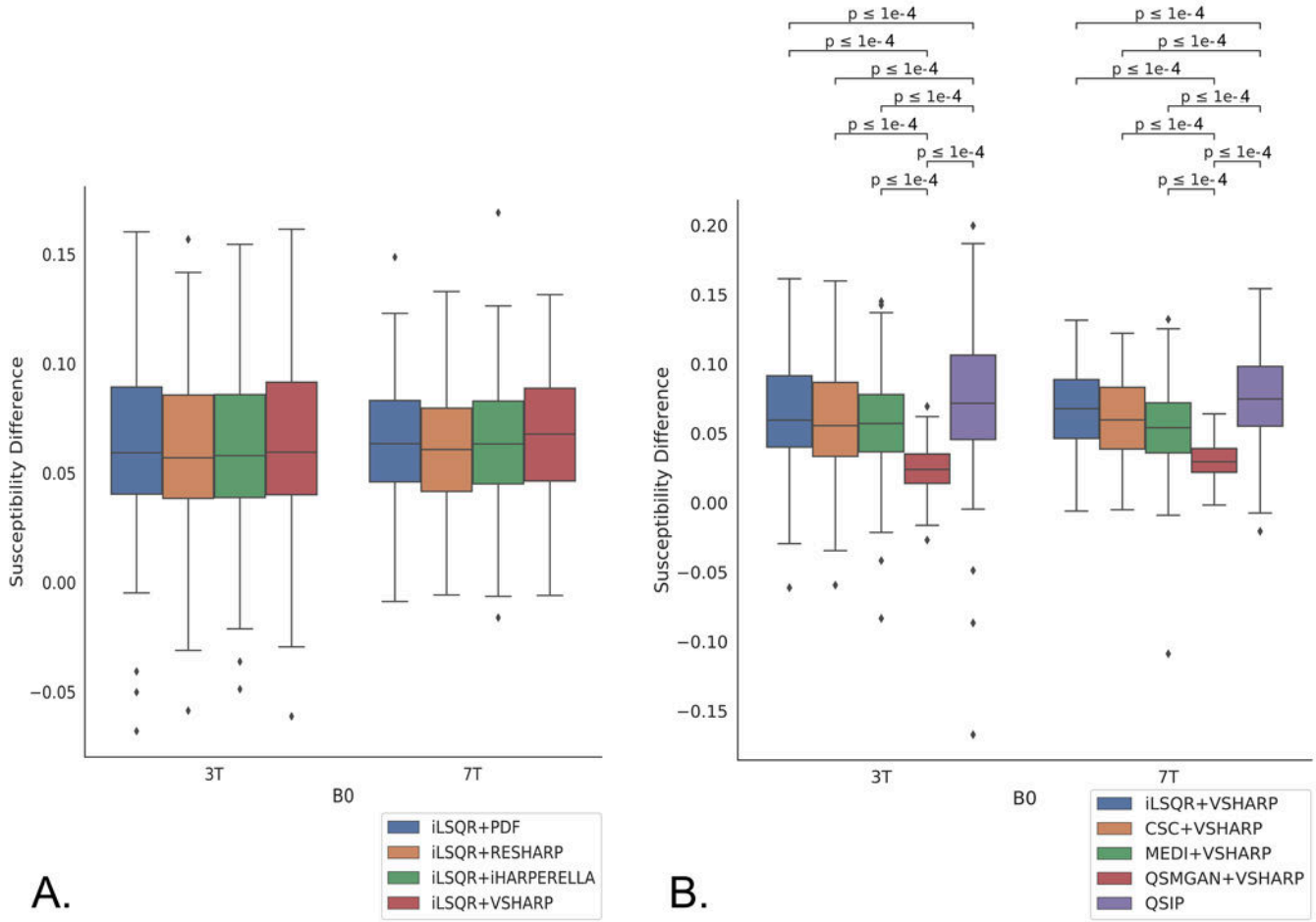

Figure 8.

Boxplots of CMB contrast at 3T and 7T. (A) Comparison among background field removal algorithms. (B) Comparison among dipole inversion methods. Lower error bars are the 25th percentile - 1.5 * IQR or the mimumum value if it is larger, while upper error bars reflect the 75th percentile + 1.5 * IQR or maximum value if it is smaller.

Author Manuscript Author Manuscript Author Manuscript Author Manuscript

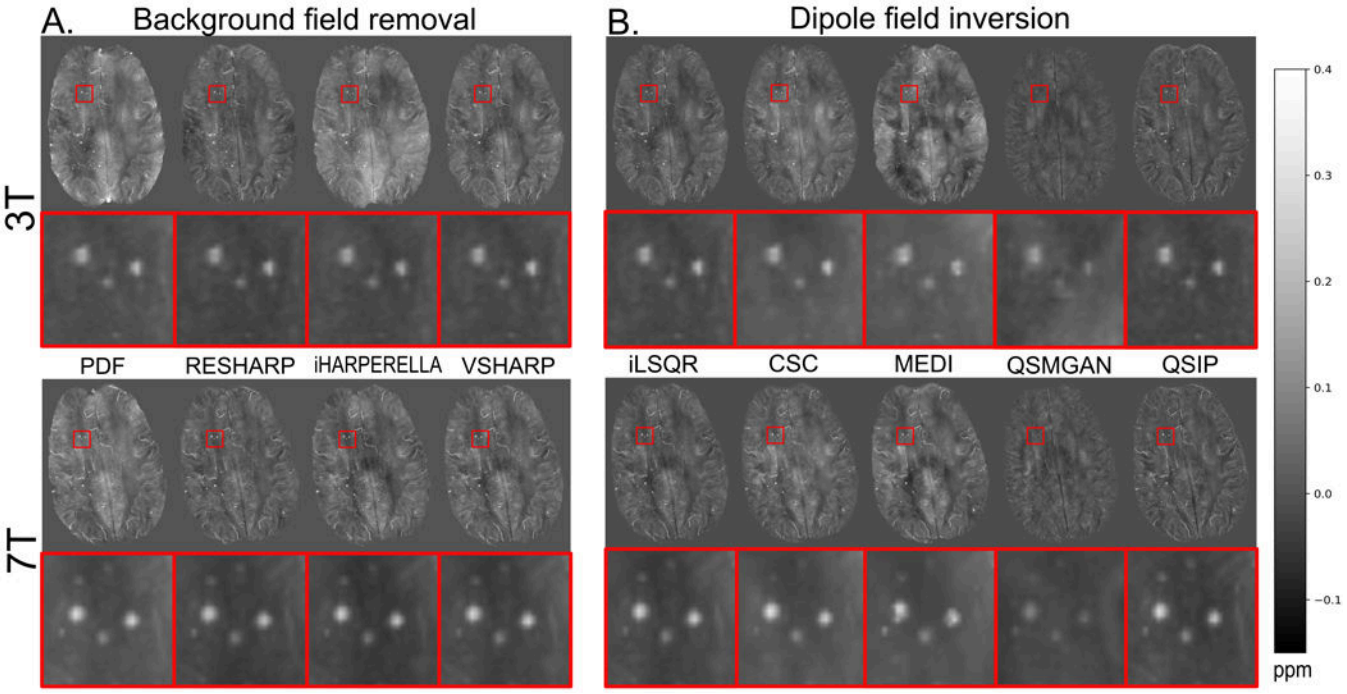

Figure 9.

Visual comparison of CMB contrast from different algorithms at 3T and 7T. Top left: background field removal algorithms at 3T. Top right: dipole inversion algorithms at 3T. Bottom left: background field removal algorithms at 7T. Bottom right: dipole inversion algorithms at 7T.

Author Manuscript

Author Manuscript

Author Manuscript

Author Manuscript

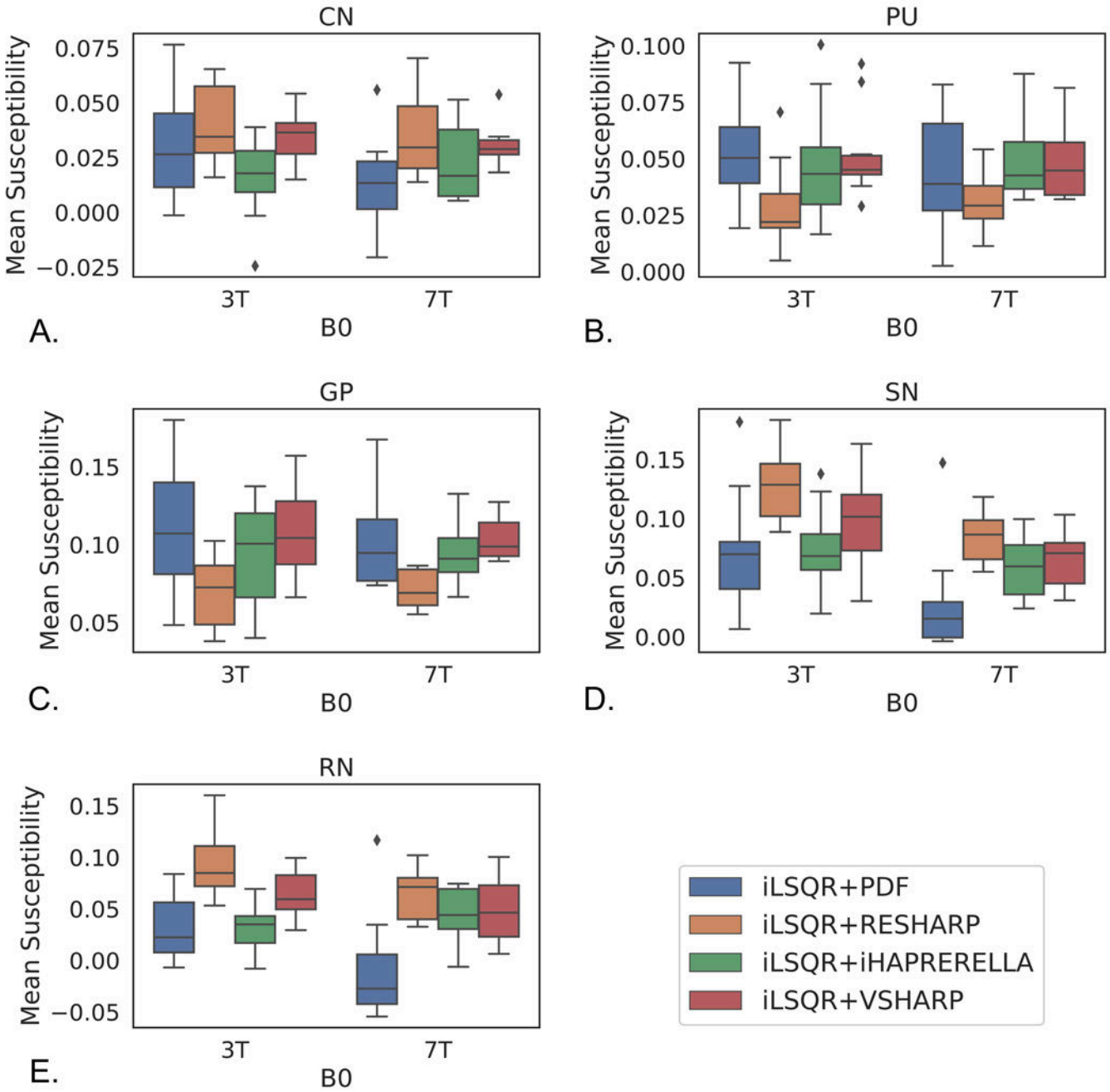

Figure 10.

Box plots comparing susceptibility values among background field removal algorithms from basal ganglia regions in patients: A. caudate nucleus (CN); B. putamen (PU); C. globus pallidus (GP); D. substantia nigra (SN); E. red nucleus (RN). Lower error bars are the 25th percentile - 1.5 * IQR or the mimumum value if it is larger, while upper error bars reflect the 75th percentile + 1.5 * IQR or maximum value if it is smaller.

Author Manuscript Author Manuscript Author Manuscript Author Manuscript

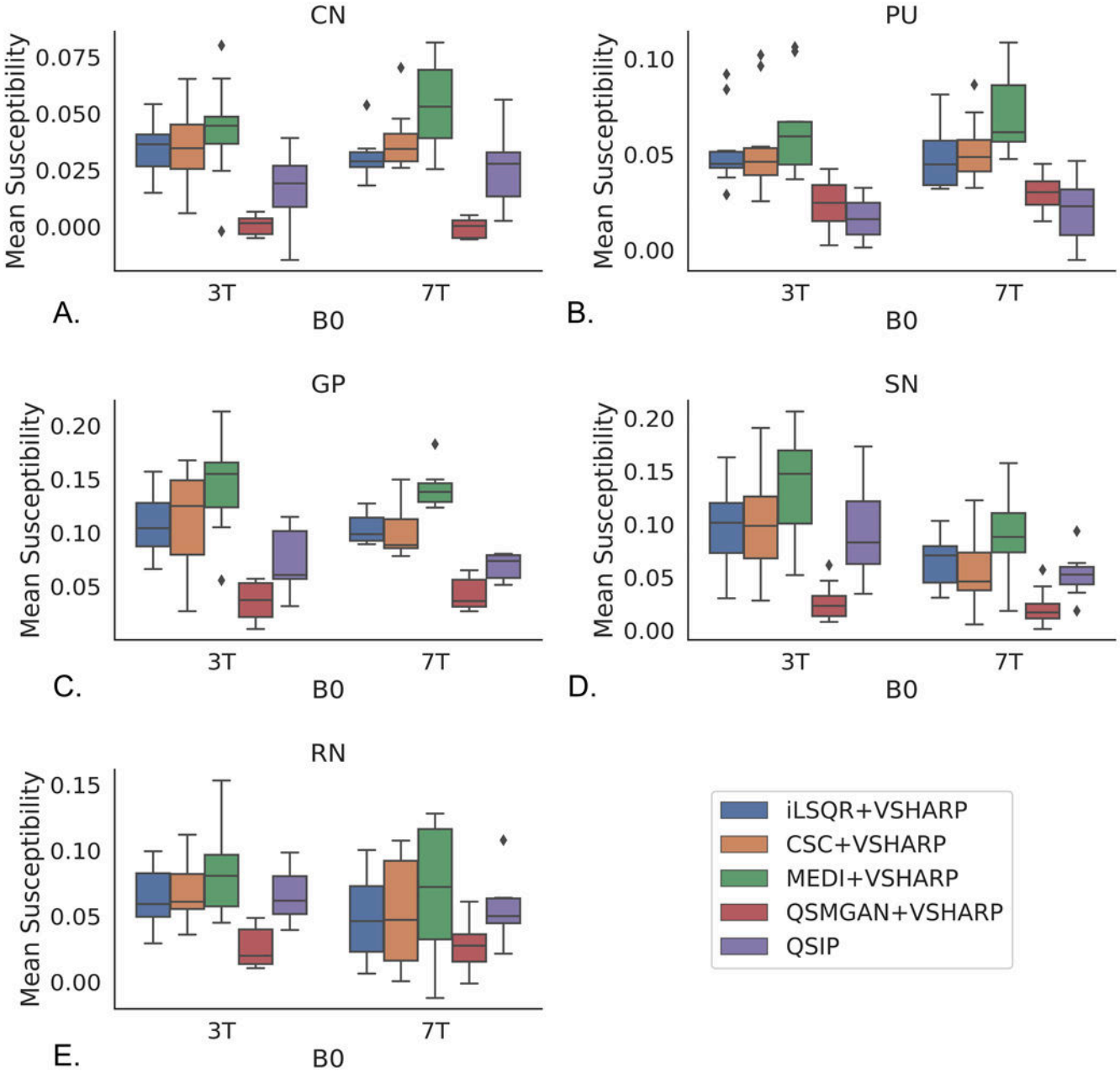

Figure 11.

Box plots comparing susceptibility values among dipole inversion methods from basal ganglia regions in patients: A. caudate nucleus (CN); B. putamen (PU); C. globus pallidus (GP); D. substantia nigra (SN); E. red nucleus (RN). Lower error bars are the 25th percentile - 1.5 * IQR or the mimumum value if it is larger, while upper error bars reflect the 75th percentile + 1.5 * IQR or maximum value if it is smaller.

Author Manuscript Author Manuscript Author Manuscript Author Manuscript

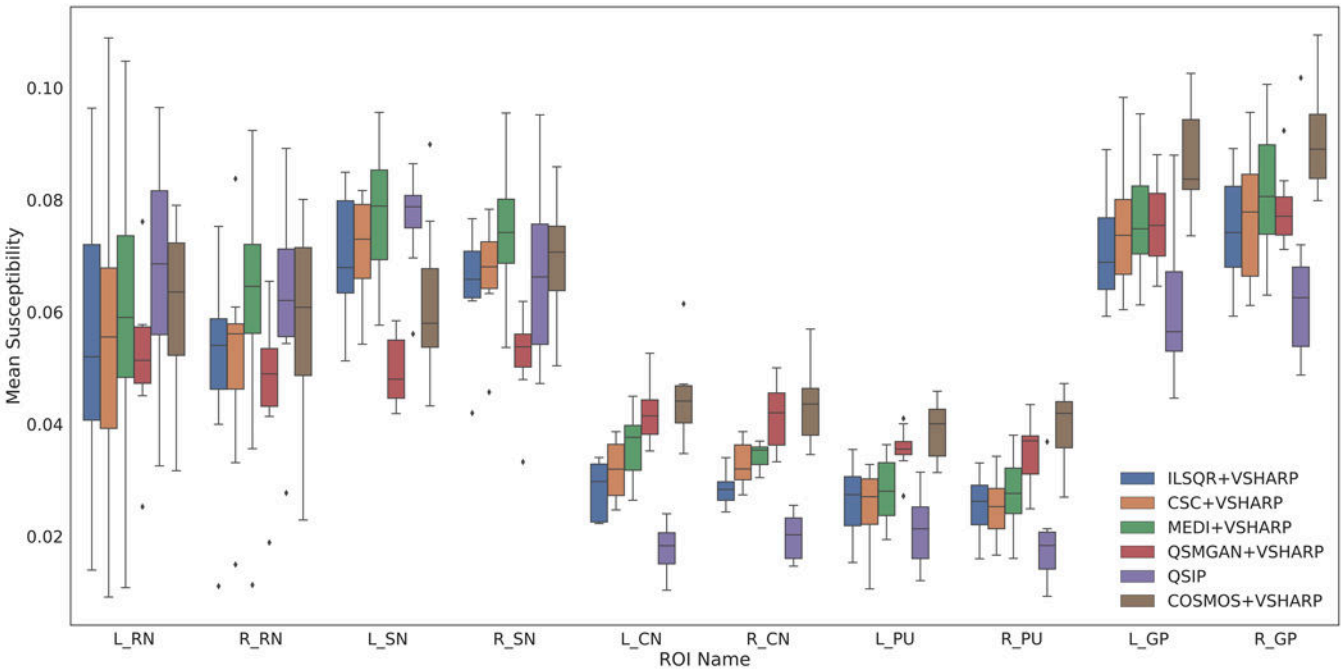

Figure 12.

Box plots comparing mean susceptibility within basal ganglia ROIs of volunteers scanned at 7T and quantified using different dipole inversion algorithms. L: left, R: right. Lower error bars are the 25th percentile - 1.5 * IQR or the mimumum value if it is larger, while upper error bars reflect the 75th percentile + 1.5 * IQR or maximum value if it is smaller.

Author Manuscript Author Manuscript Author Manuscript Author Manuscript

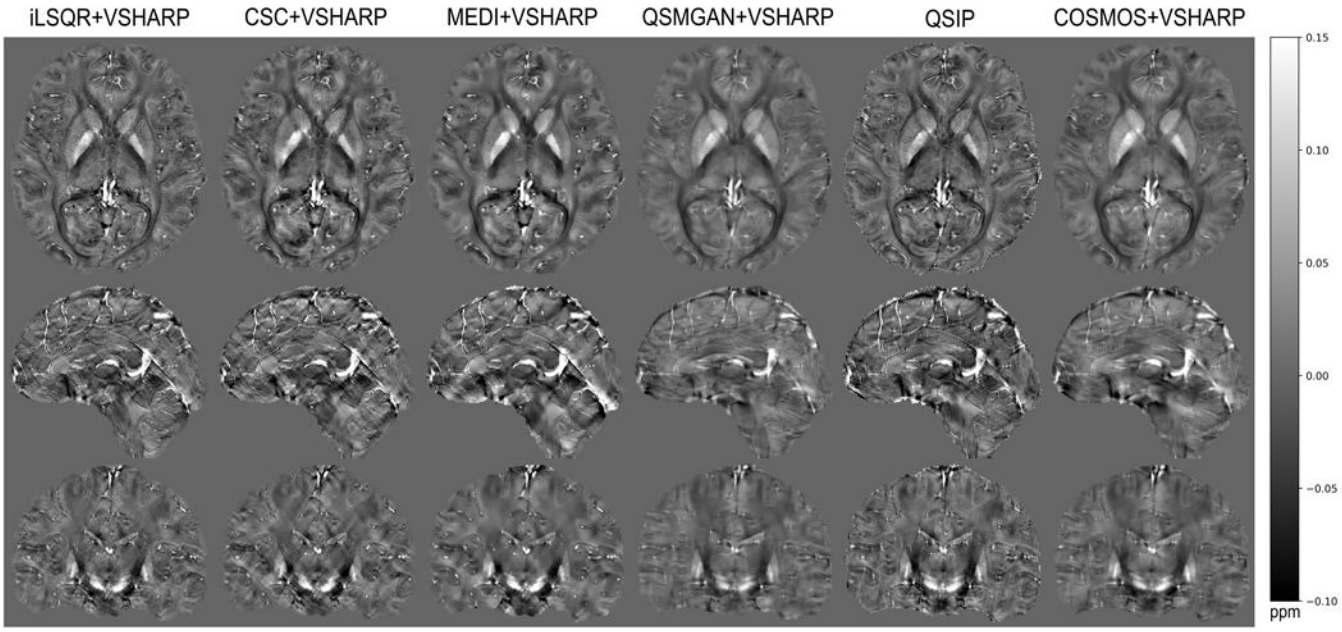

Figure 13.

Visual comparison of QSM dipole inversion algorithms of a healthy volunteer scanned at 7T (subject #5).

Author Manuscript Author Manuscript Author Manuscript Author Manuscript

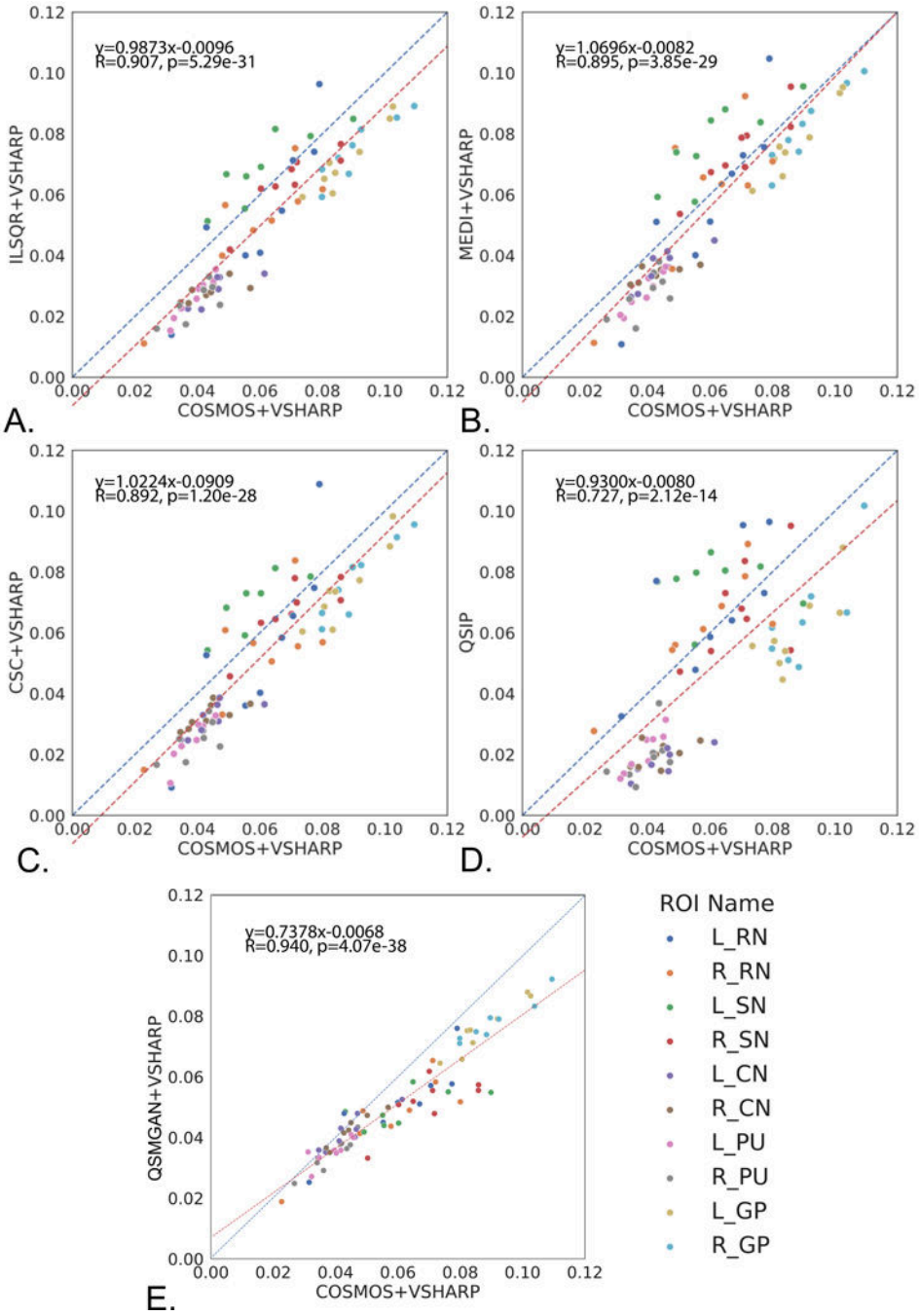

Figure 14.

Scatter and regression plots of susceptibility values for each dipole inversion method compared to COSMOS+VSHARP (blue: identity, red: linear regression)

Author Manuscript Author Manuscript Author Manuscript Author Manuscript

Table 1:
Summary of selected QSM algorithms for comparison:

Summary of selected QSM background removal and dipole inversion algorithms for comparison. The computation speed was measured on single echo sequence from group 1 patients using a work station with an AMD Opteron 6380 CPU (single core used) and 256GB memory. Approximate numbers were listed.

Background removal			
Name	**Input**	**Speed**	**Summary**
PDF	U, B	500s	Projects the total field onto a subspace spanned by background fields.
RESHARP	U, B	200s	Uses Tikhonov regularization to promote a harmonic internal field with small norm.
iHARPERELLA	L, B	50s	Uses the inverse Laplacian kernel that to project the solution of harmonic equation onto the subspace spanned by all external fields.
VSHARP	U, B	20s	Uses a combination of small and large sphere kernels when applying the SHARP property.
Dipole inversion			
MEDI	M, T, B	2,000s	Inverts the dipole convolution with regularization with anatomic image.
CSC	T, B	8,000s	Promotes image sparsity in the wavelet domain when inverting the dipole convolution.
iLSQR	T, B	100s	Uses an iterative approach to estimate the streaking artifact from ill-conditioned k-space regions only.
QSMGAN	T	34s	Uses a 3D deep convolutional neural network approach based on a 3D U-Net architecture with increased receptive field of the input phase compared to the output and Wasserstein General Adversarial Network training strategy
Integrated			
QSIP	U, B	6,000s	Inverts a perturbation model that relates phase to susceptibility in spatial domain with a tissue/air susceptibility atlas to estimate field inhomogeneity.

*U -- unwrapped phase, B -- brain mask, M -- magnitude image, L -- Laplacian image, T -- tissue phase

Author Manuscript Author Manuscript Author Manuscript Author Manuscript

Table 2:

Basal ganglia susceptibility differences among background field removal methods:

P-values of significant differences in susceptibility values of basal ganglia structures in patients scanned at 3T.

ROI	Comparison	P-Value
CN	iHARPERELLA vs VSHARP	0.007 *
PU	PDF vs RESHARP	0.007 *
GP	PDF vs RESHARP	0.009
GP	PDF vs iHAPRERELLA	0.005 *
GP	RESHARP vs VSHARP	0.009 *
GP	iHAPRERELLA vs VSHARP	0.007 *
SN	PDF vs RESHARP	0.005 *
SN	RESHARP vs iHAPRERELLA	0.005 *
SN	iHAPRERELLA vs VSHARP	0.007 *
RN	PDF vs RESHARP	0.005 *
RN	PDF vs VSHARP	0.009
RN	RESHARP vs iHAPRERELLA	0.005 *
RN	iHAPRERELLA vs VSHARP	0.007 *

* indicates statistical significance after multiple comparison correction

Author Manuscript Author Manuscript Author Manuscript Author Manuscript

Table 3:

Basal ganglia susceptibility differences among dipole inversion methods:

P-values of significant differences in susceptibility values of basal ganglia structures in patients.

ROI	Comparison	P-Value
CN	iLSQR vs QSMGAN	0.005 *
	CSC vs QSMGAN	0.005 *
	MEDI vs QSMGAN	0.005 *
PU	iLSQR vs QSMGAN	0.005 *
	iLSQR vs QSIP	0.005 *
	CSC vs QSMGAN	0.005 *
	CSC vs QSIP	0.005 *
	MEDI vs QSMGAN	0.005 *
	MEDI vs QSIP	0.005 *
GP	iLSQR MEDI	0.007
	iLSQR vs QSMGAN	0.005 *
	iLSQR vs QSIP	0.009
	CSC vs MEDI	0.007
	CSC vs QSMGAN	0.005 *
	CSC vs QSIP	0.007
	MEDI vs QSMGAN	0.005 *
	MEDI vs QSIP	0.005 *
	QSMGAN vs QSIP	0.007
SN	iLSQR vs MEDI	0.005 *
	iLSQR vs QSMGAN	0.005 *
	CSC vs MEDI	0.005 *
	CSC vs QSMGAN	0.005 *
	MEDI vs QSMGAN	0.005 *
	MEDI vs QSIP	0.005 *
	QSMGAN vs QSIP	0.005 *
RN	iLSQR vs QSMGAN	0.005 *
	CSC vs QSMGAN	0.005 *
	MEDI vs QSMGAN	0.007
	QSMGAN vs QSIP	0.007

* indicates statistical significance after multiple comparison correction

Author Manuscript

Author Manuscript

Author Manuscript

Author Manuscript

Table 4:

Whole-brain comparison metrics.

Comparison of whole-brain metrics from the 2016 QSM challenge of different dipole inversion algorithms. The best algorithm under each metric is highlighted in bold.

Method	RMSE	HFEN	SSIM
iLSQR	83.56±5.49	75.54±5.76	0.863±0.027
MEDI	101.43±5.81	97.08±7.49	**0.892±0.017**
CSC	93.85±4.92	92.34±6.06	0.848±0.025
QSMGAN	**43.66±4.33**	**48.48±4.01**	0.848±0.014
QSIP	96.49±4.68	78.92±6.34	0.869±0.011